Wiley Online Library
Early View publication on www.wileyonlinelibrary.com
(issue and page numbers not yet assigned;
citable using Digital Object Identifier – DOI)

J. Biophotonics 1–11 (2016) / **DOI** 10.1002/jbio.201500191

Journal of BIOPHOTONICS

FULL ARTICLE

Observation of an improved healing process in superficial skin wounds after irradiation with a blue-LED haemostatic device

Riccardo Cicchi[1, 2], *Francesca Rossi*[*, 3], *Domenico Alfieri*[4], *Stefano Bacci*[5], *Francesca Tatini*[3], *Gaetano De Siena*[3], *Gaia Paroli*[5], *Roberto Pini*[3], *and Francesco S. Pavone*[1, 2, 6]

[1] National Institute of Optics, National Research Council (INO-CNR), Florence, 50125, Italy
[2] European Laboratory for Non-Linear Spectroscopy (LENS), University of Florence, Sesto Fiorentino, 50019, Italy
[3] Institute of Applied Physics, National Research Council (IFAC-CNR), Sesto Fiorentino, 50019, Italy
[4] Light4tech Firenze S.r.l., Scandicci, 50018, Italy
[5] Department of Clinical and Experimental Medicine, University of Florence, Florence, 50139, Italy
[6] Department of Physics, University of Florence, Sesto Fiorentino, 50019, Italy

Received 8 July 2015, revised 19 November 2015, accepted 7 December 2015
Published online 13 January 2016

Key words: Thermal effects, blue light-emitting diodes, photocoagulation, wound healing

The healing process of superficial skin wounds treated with a blue-LED haemostatic device is studied. Four mechanical abrasions are produced on the back of 10 Sprague Dawley rats: two are treated with the blue-LED device, while the other two are left to naturally recover. Visual observations, non-linear microscopic imaging, as well as histology and immunofluorescence analyses are performed 8 days after the treatment, demonstrating no adverse reactions neither thermal damages in both abraded areas and surrounding tissue. A faster healing process and a better-recovered skin morphology are observed: the treated wounds show a reduced inflammatory response and a higher collagen content.

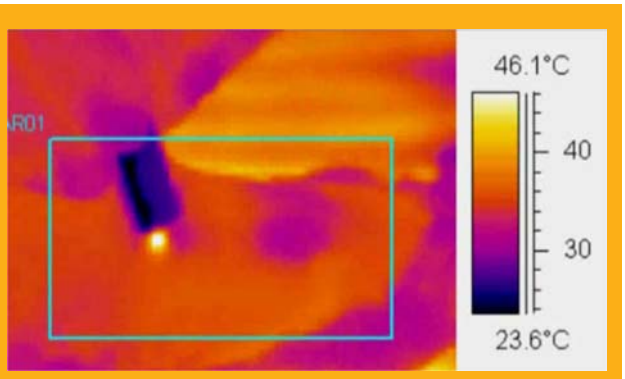

Blue LED induced photothermal effect on superficial abrasions.

1. Introduction

LED-based devices are today changing photonics applications in various research fields. This mature technology took strong advantage from the pioneering research conducted in the growth of Ga–N crystals during the 80's by Akasaki, Amano and Nakamura that brought to the invention of the blue LED [1, 2]. Such invention was extremely important because it opened the possibility of obtaining LED-based white light, with a consequent revolution of lighting applications that was recently awarded with

* Corresponding author: e-mail: f.rossi@ifac.cnr.it, Phone: +39 055 522 5337, Fax: +39 055 522 5305

Journal of BIOPHOTONICS

the Nobel Prize in Physics 2014. Since its invention in the early '90s [3–5], blue-LED technology has found several applications, including biochemical [6], and biomedical [7–10]. In fact, considering that several biological molecules and chromophores show high absorption in the UV/blue range of the spectrum, blue LED technology offers the potential of a low-cost simple source for targeting particular biological molecules. For example, when considering the absorption coefficient of skin chromophores in the UV-VIS-NIR spectrum (i.e. from 300 nm to 900 nm), haemoglobin exhibits narrow absorption peaks in the blue range (410 nm and 430 nm for oxygenated and non-oxygenated haemoglobin respectively), and its absorption coefficient is much higher than other skin chromophores [11–13]. This particular property of haemoglobin can be used to ensure a local temperature increase that is able to induce hemostasis through a photo-thermo-coagulation process. When irradiating a bleeding wound with the blue LED of proper wavelength, the light is mainly absorbed by haemoglobin naturally present in these areas, causing a local temperature increase within blood [14]. The use of proper irradiation settings in terms of fluence, irradiation time, target spot area and emission pattern allows locally inducing a temperature above the threshold for protein denaturation within blood, resulting in a fast coagulation effect [15]. The thermal effect on surrounding tissue is lower because of the reduced absorption. In other words, haemostasis is realized through a light-induced coagulation process, ensured by a spectrally selective and spatially localized photo-thermal effect [15].

Wound healing is a dynamic process that involves several molecules and cells, including mediators, blood cells, extracellular matrix, and parenchymal cells [16]. Wound healing is generally characterized by three phases overlapped in time: inflammation, tissue formation, and tissue remodelling [17]. Recent advances in cellular and molecular biology have greatly expanded our understanding of the biologic processes involved in wound repair and tissue regeneration and have led to improvements in wound care [18]. Nevertheless, wound healing remains a very complex process, difficult to understand *in toto* as demonstrated by a number of studies recently published and aimed at monitoring the process both *ex vivo* [19, 20] and *in vivo* [21, 22] using optical imaging techniques. In general, the main goal of wound care is to obtain a rapid wound healing and an aesthetically satisfactory appearance. Optical techniques, and especially LED technology, can help in reaching this goal: very recently, blue LED technology has been also tested as an improver of the wound healing process [23, 24].

In the last ten years, a blue LED photo-hemostatic device has been designed: it enables an immediate stop of the bleeding in superficial wounds (e.g. skin abrasions, oral mucosa bleeding, etc.) [25]. The goal of this preliminary study is to investigate if the blue LED treatment of superficial abrasions can affect the healing process. In order to do this, mechanical abrasions were produced on the back of 10 Sprague Dawley rats. Half of the induced wounds were treated with the blue-LED device, while the others were left to naturally recover. The induced photothermal effect was monitored during treatment by the use of a thermocamera. Visual observations, non-linear microscopic imaging, histological and immunofluorescence analyses were used to study the healing process at 8th day, in LED treated and untreated wounds.

2. Materials and methods

2.1 Blue-LED haemostatic device

The Blue-LED photo-haemostatic device has been designed and developed as part of the LighTPatcH project activities within the Biophotonics plus call 2012: it is based on the use of two commercial LEDs, emitting at 410 nm and 435 nm. These wavelengths match the main absorption peaks of haemoglobin in the blue region. The device was designed in order to be easily used in a medical application. It is a fiber-coupled device, schematically composed by: the two LED sources, having in total 1 W emission power; the electronic system for controlling LED emission conditions; the optical system, made with an optical lens in combination with a fiber coupler, for delivering LED light through an optical fiber. The light sources were mounted on a compact case, thus enabling heat dissipation towards external ambient air and easy handling (see Figure 1). Light

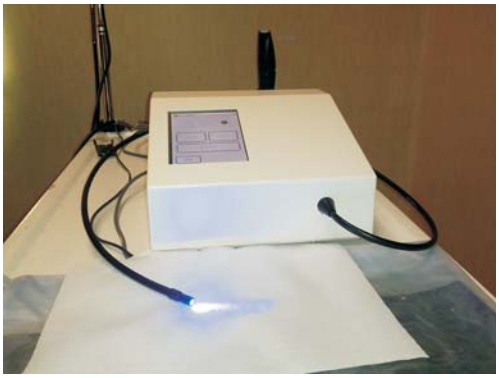

Figure 1 Photo-hemostatic device. The picture shows the optimized first LED fiber coupled photo-hemostatic device, with software control of emission power and treatment time duration.

irradiation of the skin's superficial layers was performed by placing the external surface of the photo-haemostatic fiber 1 cm far from the skin. The illuminated area thus corresponded to a circle with 5 mm radius. The resulting power densities thus was 1.27 W/cm^2. The intensity distribution of the light at the tissue surface was homogeneous, as from a top hat intensity source. During the treatment, the photo-haemostatic optical fiber was kept in motion above the wound, inducing a homogeneous thermal effect over the entire target. The optimized treatment time was 25 seconds for each wound. Only one treatment per wound was performed a few seconds after wounding.

2.2 Animal model

In this study, 10 adult male Sprague Dawley rats (Harlan Italy, weighing 200–250 g each) were used. All experiments respected the guidelines of the European Community for the care of the animals (86/609/EEC). Formal approval to conduct the experiments has been obtained from the animal subjects review board of the University of Florence. The animals were anesthetized with 3.8% Chloral hydrate (380 mg/kg i.p.) before treatment. After anaesthesia, hair removal from the back was performed and four circular areas of about 1.6 cm in diameter were identified with a non-toxic permanent marker. Four abrasions were performed within the identified areas. The abrasor consists of a drill with an extension for manual work that mounts a cylinder head of commercial sandpaper (KWH Mirka Ltd, Jeppo, Finland, 68 micron particle size). The wounds have been realized with the abrasor set at a speed of 200 rpm per minute. The rotating abrasive cylinder was brought into contact with the skin of the rat to remove it without exerting any pressure. We stopped the procedure when the underlying layer of the skin with its gaping and gushing capillaries could be observed (abrasion lasted approximately 60 s). Soon after abrasion, the two wounds on the right side were treated with the photo-hemostatic device; the two on the left side were left to heal without any treatment. During the treatment, the animals were kept at a constant temperature (37.5 °C) to reduce stress due to anaesthesia. Immediately after treatment, the wound was treated with a topical application of a small amount of Streptosil (Boehringer Ingelheim Italia spa, Milan, Italy), so as to prevent the onset of infections; all the animals were also treated with carprofen 5 mg/kg s.c. for three days. During follow up, the animals were housed in regulation cages in a controlled lighting (12/12 light and dark) and temperature facility, and had free access to water and standard rodent diet ad libitum. The animals were kept in separate cages to avoid possible infections of wounds during the healing process. After 7 days of follow up, the animals were sacrificed by humane methods and 5 samples were harvested from each animal: the two wounds treated with photo-hemostatic device, the two untreated wounds (therefore with natural healing) and a sample of healthy skin (taken from the central area of the back). The complete epithelial margins and the scab, when present, were always included in the removed wounds. The biopsies were preserved by the immediate freezing at a temperature of –80 °C and subsequently cut by use of the cryostat; the sections were then post-fixed in cold acetone and the obtained slides stored at –20 °C.

2.3 IR thermocamera observations

Direct observations of the induced superficial temperature were performed during treatment, using an infrared (IR) thermocamera. The temporal and spatial evolution of the heating in a non-contact configuration was accurately measured. The IR thermocamera (ThermoVision A20, FLIR Systems Inc., Wilsonville, OR, USA) was equipped with a 9 mm focal length germanium lens, which provided a minimum working distance of 10 cm, resulting in a spatial resolution of 0.5 mm. The camera was controlled via PC, thanks to the use of the dedicated ThermaCAM Researcher^{TM} software. Once the object parameters, such as emissivity, were provided, direct measurement of the temperature was visualized and then stored for processing in the PC. The resulting thermal sensitivity of the system was 0.12 °C at 30 °C. The skin parameters, such as its emissivity, were taken from the Refs. [26, 27]. Thermograms were used to evaluate the maximum temperature rise, the temperature spatial distribution on the skin surface, and the temperature decay time to the normal skin value at the end of the LED irradiation.

2.4 Multiphoton microscopy setup

In this study, a multiphoton microscopy setup was used for Two Photon Fluorescence (TPF) and Second-Harmonic Generation (SHG) microscopy of thin tissue cross-sections. The experimental setup consisted of a custom-built microscope, made by a compact microscopic head realized in anodized aluminium alloy that hosts the optical component. A pulsed Ti : Sapphire laser (Mira900F, Coherent, Santa Clara, US) provided the excitation pulses with 140 fs length at a repetition rate of 76 MHz and an emission wavelength of 840 nm. A few optical ele-

ments placed on the optical table served for conditioning the laser beam before entering the microscope head. In particular, a telescope collimated the laser beam, a polarization-based system allowed adjusting its power, an electronic shutter SH05 (Thorlabs, Newton, NJ, US) ensured minimal exposure of the sample. Considering that SHG signal from collagen depends on the polarization of the excitation beam [28], polarization optical elements were also used for making laser polarization circular at the sample. Inside the microscope head, laser beam was scanned with a galvanometric scanning head G1222 (Galvoline, Rome, Italy) and focused with a 20× objective lens PlanApo (Nikon, Tokyo, Japan), 0.75 NA. Fluorescence and SHG were separated from the excitation light by means of a dichroic mirror 685DCXRU (Chroma Technology Corporation, Rockingham, VT, US). SHG signal was filtered by a narrow (10 nm FWHM) band-pass filter HQ420BP (Chroma Technology Corporation, Rockingham, VT, US) and collected using a photomultiplier tube H7422 (Hamamatsu, Hamamatsu City, Japan). Fluorescence signal was collected on the same detector by removing the narrow band-pass filter and by inserting a fluorescence filter FF01-510/84-25 (Semrock, Rochester, NY, US). A detailed description of the experimental setup has been provided in [29].

2.5 Multiphoton image acquisition and analysis

Both TPF and SHG images were recorded with a pixel dwell time of 20 µs, a field of view of 400 × 400 µm^2 and a resolution of 512 × 512 pixels, using an excitation wavelength of 840 nm. Combined TPF-SHG images were presented by coding fluorescence in green and SHG in blue. FFT analysis was performed by taking SHG images of dermal collagen (about 10 images per wound) and selecting three different ROI sizes (128, 256, and 512 pixels), respectively corresponding to a ROI size of 100 µm, 200 µm and 400 µm. The FFT of each selected ROI was calculated using an ImageJ (NIH, Bethesda, US) [30, 31] built-in routine. Collagen anisotropy was then evaluated by means of the aspect ratio of the FFT profile. This parameter, corresponding to the minor to major axis ratio of the elliptic FFT profile was calculated by considering the ratio of the two eigenvalues of the covariance matrix, as described in [32]. The calculation was performed at various ROI size in order to identify the scale level at which a particular organization of collagen fibers and fiber bundles is lost [33]. Statistical student *t*-tests were done on the calculated FFT aspect ratio values at the 0.05 level ($p < 0.05$) using Microcal Origin Pro9 software (OriginLab Corporation, Northampton, US). Grey Level Co-occurence Matrices (GLCM) were calculated from SHG images according to [9] using a Matlab (Mathworks, Natick, US) routine for a neighbour index ranging from 1 to 100. GLCM Correlation was then calculated and displayed versus distance, in order to provide useful information on periodic structures or on the sudden change or regularity of a linear structure, such as breakage of a fibrillar structure [34, 35]. Mean collagen fiber bundle size was estimated on the basis of GLCM Correlation decay length, according to [36, 37].

2.6 Histology and immunofluorescence analysis

For histological evaluations, specimens were embedded in freezing tissue medium (Killik; BioOptica, Milan, Italy) and cryosections were post fixed in cold acetone. Sections from each case (one section per staining, ten microscopic fields for each sample were used for further analysis) were stained with haematoxylin and eosin or labelled with the following antigens: Heat Shock Protein (Hsp) 47 for fibroblasts [38] (Hsp47+; Abcam, Cambridge, UK), alpha Smooth Muscle Actin (SmA) for myo-fibroblasts [39] (SmA+; Sigma, Milan, Italy) by using monoclonal antibodies diluted 1 : 50 and 1 : 100, respectively. Appropriate fluorescein isothiocyanate labelled polyclonal antibodies from rabbit or mouse (1 : 32; Sigma, Milan, Italy) were used as secondary ones. Primary antibodies were applied overnight at 4 °C, secondary ones for 2 h at 37 °C. Control samples from healthy back rat skin were also used for the histological and fibroblast-targeted immunofluorescence examination. Omission of the primary antibody and substitution with an irrelevant one was used as control for the immunofluorescence reactions. Sections were photographed using a Leica optical microscope, equipped with a camera connected to a PC, and images visualized with ProgRes Capture Basic software (Jenoptik, Jena, Germany) or a WWR international PBI light microscopy plugged with a tablet camera system (Bergamo, Italy) or a Zeiss Axioskop microscope suitable for epifluorescent equipped with a digital camera (Zeiss, Jena, Germany) connected with a PC (ED, Rome, Italy) hosting the software Axiovision 4 (Zeiss, Jena, Germany). Confocal analysis was performed using a Leica Sp8 microscope (Leica, Mannheim, Germany) and a Leica 3D visualization software. All measurements were performed at the end of the experiment in blinded fashion by researchers not involved in wound preparation and treatment.

2.7 Morphometry and statistics

For studying epithelization, wounds were digitally photographed at magnification × 25 and the maximum epidermal thickness was measured in 10 epidermal tracts per specimens using the software image analysis Image J (National Institutes of Health, Bethesda, MD) [40].

Cellular infiltration as shown in haematoxylin and eosin stained sections was graded on a 0–3 arbitrary scale for each biopsy site [41, 42]. Immunostained sections, one time were placed on the microscopic stage; adjacent, not overlapping fields were photographed separately for the dermis, at magnification 40×. Hsp47+, SmA+ were counted using the software image analysis Image J as it follows. The background grey level was measured, the threshold was set at 1.5 times the background and the structures in the dermis that were brighter (i.e. more intensely fluorescent) than the threshold were counted by the software. Each image of the shape of HSP47 or SMA positive cells was subtracted from a background image to compensate for any unevenness in the illumination and camera response. The resulting image was converted into a binary image by selecting a threshold level. The image was then compared with the original optical image and any selections not corresponding to single cells were removed (see Figures 2 and 3) [43, 44]. The counts were obtained for spots larger than 50 pixel, which were assumed to represent whole cells. For each comparison, the average value for each specimen was assumed as a sample unit.

All differences were subjected to analysis of variance (including Bonferroni-corrected *t*-tests or Tukey HSD tests), assuming $p < 0.05$ as significant, using StatView 512+ (Abacus Concepts, Berkeley, CA) or StatPlus (AnalystSoft, Walnut, CA) programs. In case of significant result of the analysis of variance among all experimental groups, the values at each time point were compared with controls by Student *t*-test for unpaired values with two tails, assuming $p < 0.05$ as significant [45].

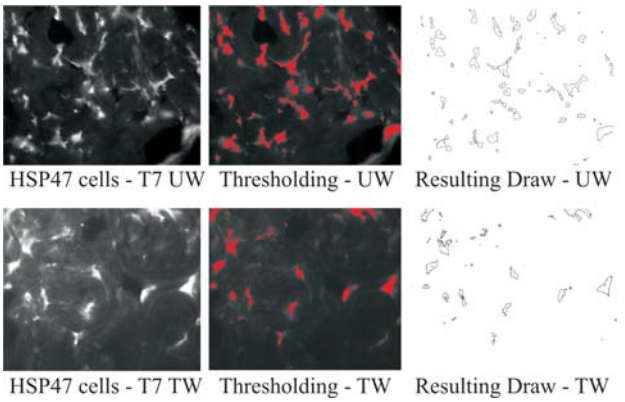

Figure 2 Representative digitized image of fibroblasts in untreated or treated wound with enhanced threshold and consequent drawing image after disappearance of residual noise.

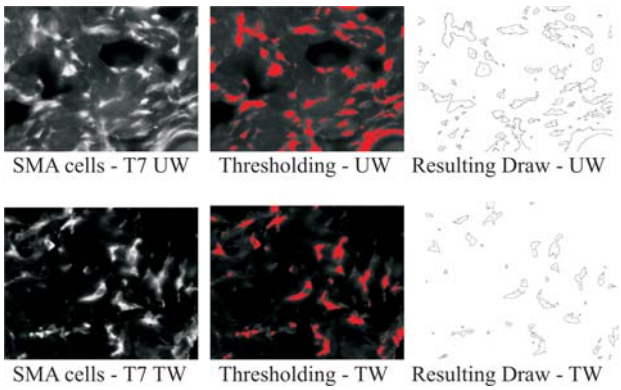

Figure 3 Representative digitized image of myofibroblasts in untreated or treated wound enhanced threshold and consequent drawing image after disappearance of residual noise.

3. Results

3.1 Direct observation during treatment

Thermal analysis during treatment evidenced that there is an immediate temperature enhancement in the irradiated bleeding area: a maximum temperature rise of 13.3 ± 3.1 °C (corresponding to an external wound site temperature of about 48.3 °C) is reached in the first 5 seconds and it is maintained almost constant for 20 s. No thermal damage to surrounding intact tissues was observed. No collateral effects were evidenced during treatment.

3.2 Direct observations during follow up

The wounds had an initial mean area of 2 cm^2 (see Figure 4A), calculated with the assumption that the wounds were a circle of about 16 mm in diameter. The aspect of the wounds, including the absence of new hair growth and signs of the initial abrasion (excluding healed surface areas), was re-evaluated after 7 days to assess the effect of the treatments on the healing process (Figure 4B).

3.3 Combined TPF-SHG imaging

The microscopic imaging was performed on thin skin tissue cross-sections extracted from both treated

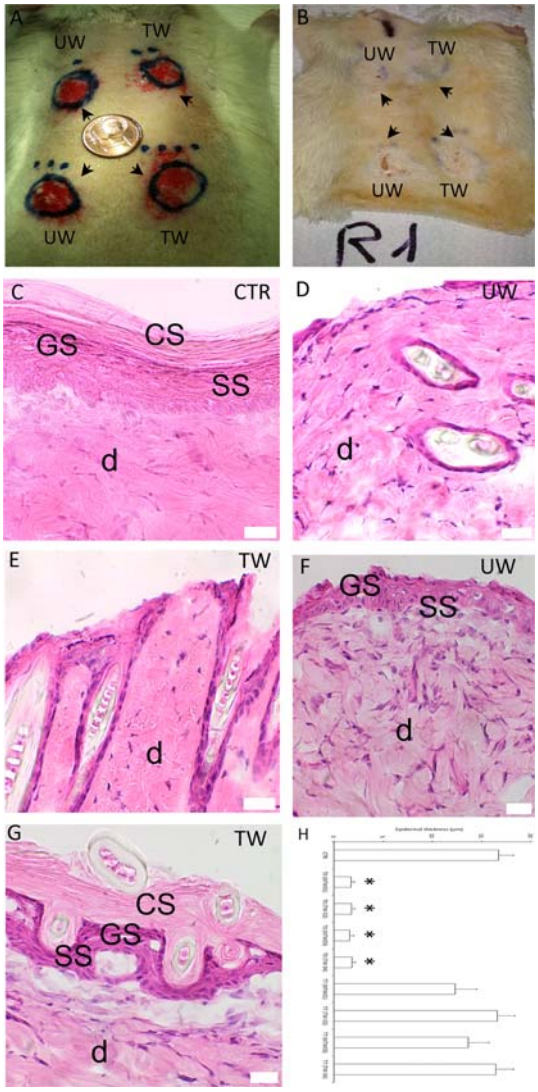

Figure 4 Representation of different steps during the study of epithelization: grossly evaluation of wounds soon after the treatment (**A**) and at 7 days after treatment (**B**); H & E images of (**C**) a control, (**D**, **E**) an abrasion evoked by initial treatment with a consequent disappearance of epidermis in untreated or treated wound, (**F**, **G**) the appearance of epidermis in treated but not in untreated wound with the use of bar graphs (**H**), representing the mean and SE of the thickness of epidermis at the two time steps. Corneum stratum (CS), granular stratum (GS) and spinous stratum (SS) are evident in C and G, only GS and SS in F.

wound (TW) and untreated wound (UW) areas from the animals used in the study. Both TPF and SHG images were acquired using the same excitation wavelength (840 nm) and presented by coding fluorescence in green and SHG in blue, as shown in the example represented in Figure 5.

In particular, the combined TPF-SHG images are represented on the left for both UW (Figure 5A) and TW (Figure 5D). The difference in terms of dermal morphology is clearly distinguishable from the images, and is even more pronounced by separating TPF and SHG channels. TPF images are represented in the middle column for both UW (Figure 5B) and TW (Figure 5E). The images show that in the UW the inflammatory response is still ongoing, as demonstrated by the large presence of vessels and cells in the dermis. On the other hand, only few cells are visible in the TW area and most of the fluorescence signal originating from dermis is due to the presence of elastic fibers [46]. In both UW and TW, the epidermal morphology is fully recovered, as demonstrated by the comparable epidermis thickness and keratinocyte density in the two areas.

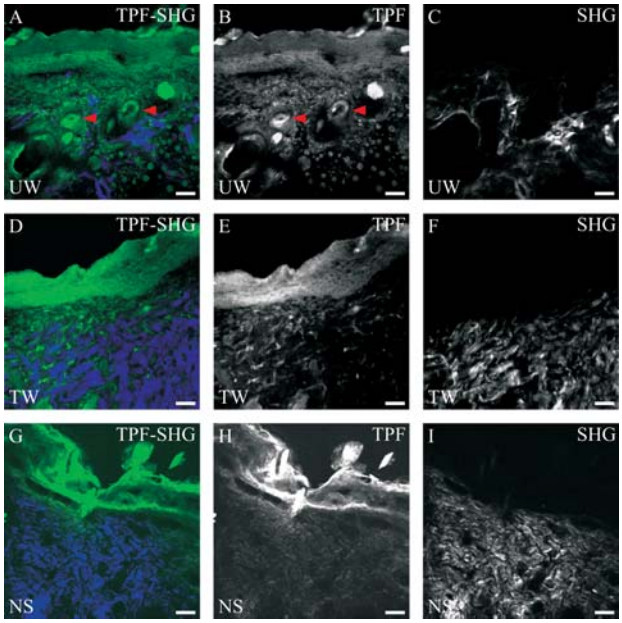

Figure 5 Combined TPF-SHG imaging. On the left, combined TPF-SHG images of thin tissue cross sections excised from untreated wound areas (**A**), treated wound areas (**D**), and normal skin (**G**). Fluorescence is coded in green colour scale and SHG is coded in blue colour scale. In the middle, TPF images of thin tissue cross sections excised from untreated wound areas (**B**), treated wound areas (**E**), and normal skin (**H**). On the right, SHG images of thin tissue cross sections excised from untreated wound areas (**C**), treated wound areas (**F**), and normal skin (**I**). Scale bars: 40 μm.

However, in the UW area there is still the presence of crusts, as resulted by the bright signal in some regions beneath the epidermal surface. This datum has been also verified by visually observing images during acquisition. SHG images are represented in the right column for both UW (Figure 5C) and TW (Figure 5F).

Here the differences between UW and TW are even more pronounced. The amount of collagen is much higher in the TW area with respect to the UW area. Collagen distribution is more sparse in the UW area, whereas is more uniform in the TW area,

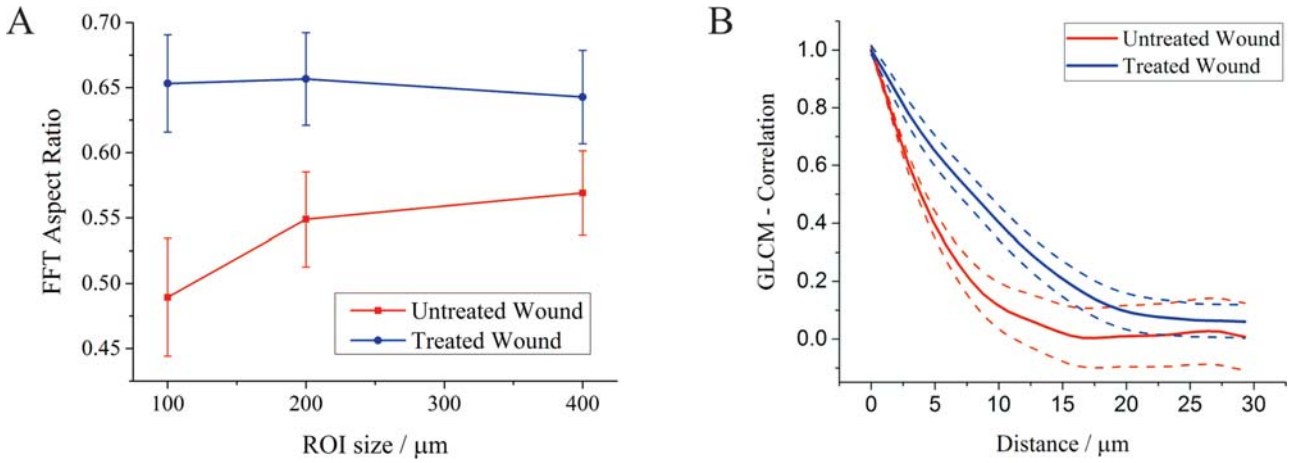

Figure 6 SHG image analysis. (**A**) FFT Aspect Ratio plotted versus ROI size for both UW (red line) and TW (blue line) areas. (**B**) GLCM – Correlation versus distance, averaged over all the examined ROIs, for both UW (red line) and TW (blue line) areas. Plain lines correspond to the average over all the examined samples; dashed lines represent the average plus (or minus) SD, calculated over all the examined samples.

where collagen almost fill the dermal space, as commonly occurs in healthy dermis [47]. Collagen orientation is quite different as well, with TW showing a more isotropic distribution of collagen fiber bundles with several intersections in comparison to UW where intersections are not clearly identifiable yet. Two different image analysis methods have been used for analysing SHG images and quantify the morphological differences observed, as described in the following section.

3.4 Image pattern analysis on SHG images of collagen

SHG images were analyzed using two different image pattern analysis methods, respectively aimed at characterizing the orientation anisotropy of collagen fiber bundles and their average size. The orientation anisotropy was determined by processing SHG images with an FFT routine on ROIs of different sizes (100 micrometers, 200 micrometers, and 400 micrometers). The Aspect Ratio of the FFT was taken as indicator of collagen anisotropy. The obtained results, averaged on all the examined ROIs, are plotted in Figure 6A for a ROI size of 100, 200, and 400 micrometers.

Hence, in TW areas collagen fiber bundles have a more isotropic distribution while in UW areas the distribution is more anisotropic. In addition, the FFT Aspect Ratio showed a different dependence on the ROI size for UW and TW, with a constant behaviour for TW and an increase for UW. This means that independently on the length scale selected for FFT analysis, TW areas showed increased values with respect to UW areas.

The typical size of a collagen fiber bundle was evaluated by calculating the GLCM-Correlation value as a function of the neighbour index (Figure 6B) and its typical decay length. The profiles for GLCM-Correlation decay, averaged for all the examined ROIs, are shown in Figure 6B. The faster decay observed in UW with respect to TW indicates a smaller typical size for a collagen fiber bundle in UW, while a larger typical size in TW.

3.5 Histology and immunofluorescence examination

In order to evaluate the epithelization and the extent of the inflammatory reaction in untreated and treated wounds, the hematoxylin-eosin staining was performed. The epidermal measurements of TW and UW groups and control groups are presented in Figure 4. After the excision the epidermal surface TW and UW groups was completely lost (Figure 4E and Figure 4D). After 7 days from the treatment, while in TW group every layer of epidermis was completely regenerated (Figure 4F), in UW group the stratum corneum was still to be formed (Figure 4G).

The light microscopy evaluation of stained section of dermis in UW showed a rich cellular infiltrate (Figure 7B). In comparison with UW, sections of TW tissue showed, by examination of grading scale, a significant decrease (50% reduction, $p < 0.05$) of inflammatory cellular infiltration (Figure 7C). The level of inflammatory cellular infiltration in TW was found closer to the one found in a control sample than in of UW (Figure 8). To determine whether the population of the cellular types involved in wound healing were different in UW and TW, light micro-

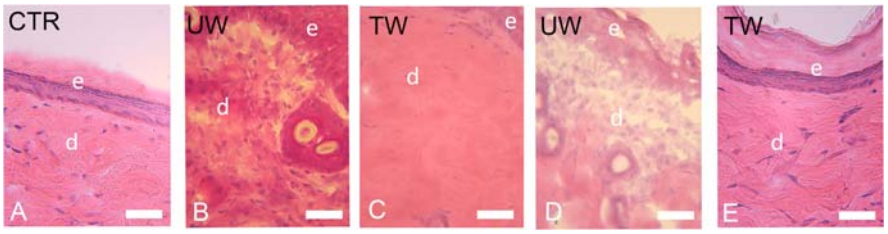

Figure 7 Histological examination. H & E images of subpapillary cell infiltrate in control (**A**), wounded (**B**–**D**), and treated skin (**C**–**E**). In the images both epidermis (e) and dermis (d) are visible.

scopy and immunofluorescence analysis were performed. The presence of fibroblasts and myofibroblasts was assessed.

At light microscopy, in the dermis of UW, spindle shaped fibroblasts-like cells were recognizable by basophil cytoplasm (data not shown). At fluorescence microscopy, these cells were easily demonstrated to be fibroblasts by HSP47 expression (Figure 9). As shown by morphometric analysis (Figure 8, middle), the density of HSP47 positive cells in TW was significantly reduced ($p < 0.005$) of about a half and was comparable to the fibroblasts density found in a control sample. Myofibroblasts were also identified, by the expression of SMA, in both TW and UW (Figures 8 and 10). In the dermis of TW we revealed a reduction of these cells that was similar to the fibroblasts decrease (50%, $p < 0.05$), as shown in Figure 8.

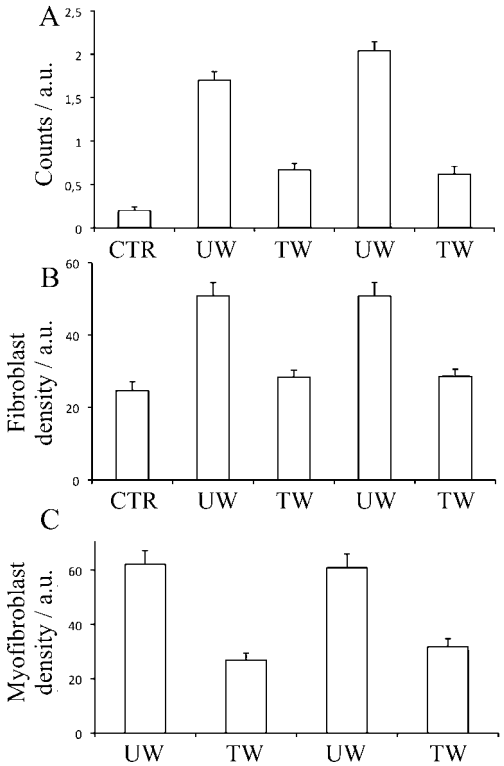

Figure 8 Bar graphs representing mean and SE of cellular infiltration (for each biopsy site) in a 0–3 arbitrary scale (top); mean and SE of HSP47 (middle) and SMA (bottom) in untreated or treated wounds.

The results obtained with fluorescence microscopy were further confirmed by confocal microscopy. Both HSP47 and SMA expressions, to reveal the presence of fibroblasts and myofibroblast, were assessed in TW and UW and a qualitative three-dimensional analysis was performed. Figure 11 shows representative images in which the reduction of both fibroblasts and myofibroblast can be appreciated.

4. Discussion

The blue LED photohaemostatic device is able to induce a temperature rise in a bleeding wound, close to the denaturation temperature of blood proteins. No thermal damage is induced in the healthy, surrounding tissue. The device can thus be used to treat superficial abrasions, to induce a fast and selective coagulation effect. All the obtained results suggested an improved wound healing process in TW with respect to UW. In fact, visual observation indicated that, from 4–5 days, skin recovery is at a later stage in TW with respect to UW. We can interpret this result in terms of an improved healing process in TW with respect to UW. However, it is not yet clarified if the effect on skin appearance is due to light-tissue interaction or just to a faster crusts loosening in TW because of the haemostasis induced at an early stage. Non-linear microscopic analysis helped in determining the effect at a dermal level. We found a higher amount of collagen fiber bundles more intertwined in TW with respect to UW. This datum was reproducible in all the examined samples and is probably an indication of the fact that production of new collagen started earlier in the TW, so that the normal dermal collagen organization is recovered in TW after 8 days whereas it is not yet recovered in the UW. In fact, a higher amount of collagen fiber bundles more intertwined in TW with respect to UW could reflect a faster neocollagenesis occurring in TW with respect to UW. We also found a quite different collagen organization in the two types of samples.

TW areas showed collagen fiber bundles with various orientations, forming the intersections of typical dermal collagen architecture. On the other hand, in UW areas, collagen fiber bundles were not uniformly oriented and their intersections were not

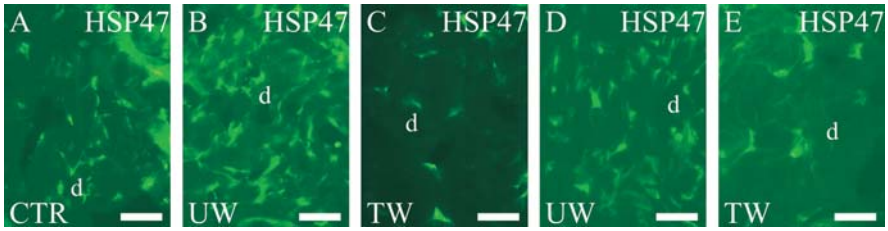

Figure 9 Histochemical examination. Localization of HSP47 positive cells in control (**A**), untreated (**B**, **D**) or treated (**C**, **E**) wounds. The images visualize the dermis (d) of the four wounds in a same animal model.

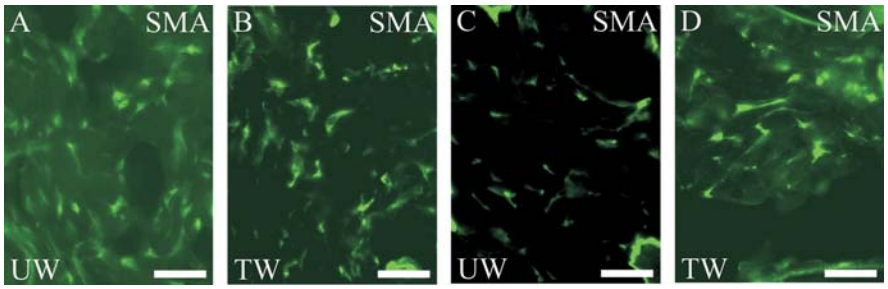

Figure 10 Histochemical examination. Localization of SMA positive cells in untreated (**A**, **C**) or treated (**B**, **D**) wounds. The images visualize the dermis (d) of the four wounds in a same animal model.

clearly identifiable yet. In addition, in TW collagen organization was more isotropic and not dependent on the ROI size, whereas in UW collagen organization becomes more isotropic as the ROI size increases. Finally, we found that collagen fiber bundle size is in average smaller in the UW with respect to the TW. These results provided additional proof of a faster healing process. The larger fiber bundle size and the higher isotropy observed in TW could be due to a more mature and organized collagen architecture in TW with respect to UW. Histology demonstrated that epithelization process was completed in TW group but not in UW group; in particular in TW group the epidermis was completed in all the layers and his thickness reached normal values [48]. Besides the inflammatory response, still ongoing after 8 days, in TW is strongly reduced with respect to UW. This provides further support to the hypothesis of a faster wound healing. Immunofluorescence analyses demonstrated a lower density of dermal cells as fibroblasts and myofibroblasts in TW, face to a higher density in UW, suggesting that the inflammatory response associated with the wound healing is still ongoing in UW, while it seems to be shortened in TW.

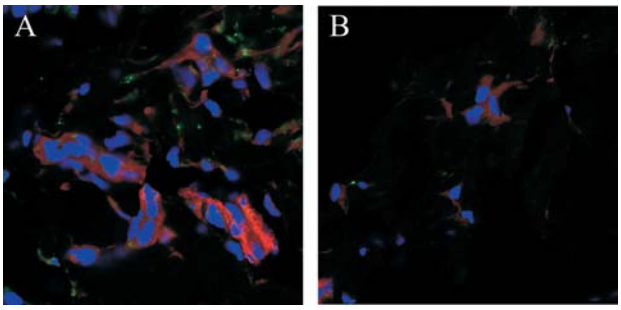

Figure 11 Confocal examination. Localization of cell nuclei (DAPI, blue), fibroblast (HSP47, green) and myofibroblast (alpha SMA, red) in untreated (**A**) or treated (**B**) wounds.

5. Conclusions

In conclusion, a faster wound healing process was found in treated abrasions with respect to the control wounds. Visual observations, non-linear microscopic imaging, and histological/histochemical analyses pointed out that after 8 days from treatment the wounds showed a higher collagen content, a better recovered morphology and organization of dermal collagen, minimal inflammatory response, no adverse reaction neither thermal damage in both wound areas and surrounding tissue. All the results obtained from these analyses constitute a strong support to the hypothesis that the selective photo-thermal effect used for inducing haemostasis in superficial skin wounds is associated to a faster healing process.

Acknowledgements The research leading to these results has received funding from Tuscany Region and EU FP7 BiophotonicsPlus projects "LighTPatcH" (Led Technology in Photo Haemostasis) and "LITE" (Laser Imaging of The Eye), from the European Union Seventh Framework Programme (FP7/2007–2013) under grant agreement number 284464, from the Italian Ministry of Health (GR-2011-02349626), from the Italian Ministry for Education, University and Research in the framework of the Flagship Project NANOMAX, from Fondazione Pisa, and from Ente Cassa di Risparmio di Firenze.

Author biographies Please see Supporting Information online.

References

[1] I. Akasaki, H. Amano, and K. Hiramatsu, Inst. Phys. Conf. Ser. **91**, 633–636 (1988).
[2] H. Amano, M. Kito, K. Hiramatsu, and I. Akasaki, Jpn. J. Appl. Phys. Part 2-Letters **28**, L2112–L2114 (1989).
[3] H. Amano, T. Asahi, and I. Akasaki, Jpn. J. Appl. Phys. **29**, L205–L206 (1990).
[4] H. Amano, M. Kitoh, K. Hiramatsu, and I. Akasaki, JES **137**, 1639–1641 (1990).
[5] I. Akasaki, H. Amano, M. Kito, and K. Hiramatsu, J. Lumin. **48–49**, 666–670 (1991).
[6] F. Xu, Z. Lv, X. Lou, Y. Zhang, and Z. Zhang, Appl Optics **47**(29), 5337–5340 (2008).
[7] Y. L. Qin, X. L. Luan, L. J. Bi, Z. Lue, Y. Q. Sheng, G. Somesfalean, C. N. Zhou, and Z. G. Zhang, Photochem Photob B-Biology **87**(2), 88–94 (2007).
[8] M. C. Bandeca, O. El-Mowafy, E. G. Saade, A. N. S. Rastelli, V. S. Bagnato, and S. T. Porto-Neto, Laser Physics **19**(5), 1050–1055 (2009).
[9] H. C. Wang and Y. T. Chen, Opt Express **20**(9), 10186–10199 (2012).
[10] N. G. Yeh, C. H. Wu, and T. C. Cheng, Renewable and Sustainable Energy Reviews **14**(8), 2161–2166 (2010).
[11] M. J. C. Van Gemert, S. L. Jacques, H. J. C. M. Sterenborg, and W. M. Star, IEEE Trans. Biomed. Eng. **36**, 1146–1154 (1989).
[12] J. Mobely and T. Vo-Dinh, Optical properties of Tissue, in Biomedical Photonics Handbook, T. Vo-Dinh ed. (CRC Press, Boca Raton, 2003).
[13] A. N. Bashkatov, E. A. Genina, V. I. Kochubev, and V. V. Tuchin, J. Phys. D: Appl Phys **38**(15), 2543–2555 (2005).
[14] Z. Tarle, A. Meniga, A. Knezevic, J. Sutalo, M. Ristic, and G. Pichler, J. Oral. Rehabil. **29**(7), 662–667 (2002).
[15] M. H. Niemz, Laser-Tissue Interactions (Springer Verlag, Berlin, 1996).
[16] P. Martin, Science **276**(5309), 75–81 (1997).
[17] A. J. Singer and R. A. F. Clark, New Engl. J. Med. **341**, 738–746 (1999).
[18] S. J. Forbes and N. Rosenthal, Nat. Med. **20**(8), 857–869 (2014).
[19] A. T. Yeh, B. Kao, W. G. Jung, Z. Chen, J. S. Nelson, and B. J. Tromberg, J. Biomed. Opt. **9**(2), 248–253 (2004).
[20] T. J. Wang, W. Lo, C. M. Hsueh, M. S. Hsieh, C. Y. Dong, and F. R. Hu, J. Biomed. Opt. **13**(3), 034019 (2008).
[21] S. Lange-Asschenfeldt, A. Bob, D. Terhorst, M. Ulrich, J. Fluhr, G. Mendez, H. J. Roewert-Huber, E. Stockfleth, and B. Lange-Asschenfeldt, J. Biomed. Opt. **17**(7), 076016 (2012).
[22] G. Deka, W. W. Wu, and F. J. Kao, J. Biomed. Opt. **18**(6), 61222 (2013).
[23] N. Adamskaya, P. Dungel, R. Mittermayr, J. Hartinger, G. Feichtinger, K. Wassermann, H. Redl, and M. Van Griensven, Injury **42**(9), 917–921 (2011).
[24] B. Hochman, C. E. Pinfildi, M. A. Nishioka, F. Furtado, S. Bonatti, P. K. P. Monteiro, A. S. Antunes, P. R. Quieregatto, R. E. Liebano, G. Chadi, and L. M. Ferreira, Lasers Med. Sci. **29**(3), 1203–1208 (2014).
[25] F. Rossi, R. Pini, G. De Siena, D. Massi, F. S. Pavone, D. Alfieri, and G. Cannarozzo, Proc. SPIE **7548**, 754807 (2010).
[26] T. Togawa, Clinical Physics and Physiological Measurement **10**, 39–48 (1989).
[27] J. Huang and T. Togawa, Physiological Measurement **16**, 295–301 (1995).
[28] S. Psilodimitrakopoulos, P. Loza-Alvarez, and D. Artigas, Biomed Opt Express **5**, 4362–4373 (2014).
[29] R. Cicchi, D. Kapsokalyvas, and F. S. Pavone, BioMed research international **2014**, 903589 (2014).
[30] W. S. Rasband and J. Image, U.S. National Institutes of Health, Bethesda, Maryland, USA, 1997–2012 (http://imagej.nih.gov/ij/).
[31] C. A. Schneider, W. S. Rasband, and K. W. Eliceiri, Nat. Methods **9**, 671–675 (2012).
[32] R. Cicchi, D. Kapsokalyvas, V. De Giorgi, V. Maio, A. Van Wiechen, D. Massi, T. Lotti, and F. S. Pavone, Journal of biophotonics **3**, 34–43 (2010).
[33] R. Cicchi, N. Vogler, D. Kapsokalyvas, B. Dietzek, J. Popp, and F. S. Pavone, Journal of Biophotonics **6**, 129–142 (2013).
[34] R. Cicchi, D. Kapsokalyvas, M. Troiano, P. Campolmi, C. Morini, D. Massi, G. Cannarozzo, T. Lotti, and F. S. Pavone, Journal of Biophotonics **7**(11–12), 914–925 (2014).
[35] R. Cicchi, C. Matthaus, T. Meyer, A. Lattermann, B. Dietzek, B. R. Brehm, J. Popp, and F. S. Pavone, Journal of Biophotonics **7**, 135–143 (2014).
[36] R. Cicchi, D. Kapsokalyvas, V. De Giorgi, V. Maio, A. Van Wiechen, D. Massi, T. Lotti, and F. S. Pavone, Journal of Biophotonics **3**, 34–43 (2010).
[37] R. Cicchi, C. Matthäus, T. Meyer, A. Lattermann, B. Dietzek, B. R. Brehm, J. Popp, and F. S. Pavone, Journal of Biophotonics **7**, 135–143 (2014).
[38] T. Goodpaster, A. Legesse-Miller, M. R. Hameed, S. C. Aisner, J. Randolph-Habecker, and H. A. Coller, Journal of Histochemistry and Cytochemistry **56**, 347–358 (2008).
[39] G. Gabbiani, Journal of Pathology **200**, 500–503 (2003).
[40] L. Florin, J. Knebel, P. Zigrin, B. Vonderstrass, C. Mauch, M. Schorpp-Kistner, A. Szaboski, and P. Angel, J. Invest. Dermatol. **126**(4), 902–911 (2006).
[41] A. Bonelli, S. Bacci, and G. A. Norelli, Int. J. Leg. Med. **117**(6), 331–334 (2003).
[42] Y. Nishimura, M. Li, G. Qin, H. Hamada, J. Asai, H. Takenaka, H. Sekiguchi, M. A. Renault, K. Juio, N. Katoh, S. Kishimoto, A. Ito, C. Kamide, J. Kenny, M. Millay, S. Misener, T. Thorne, and D.W. Losordo, J. Invest. Dermatol. **132**(3), 711–720 (2012).
[43] M. Hall-Beyer, the GLCM tutorial, version 2.10 (accessed 2007) (http://www.fp.ucalgary.ca/mhallbey/tutorial.htm).
[44] M. Mickalik, M. Pierzchalska, A. Legutko, M. Ura, A. Ostaszewska, J. Soja, and M. Sanak, Med. Sci. Monit. **15**(7), 194–201 (2009).

[45] S. Bacci, B. De Fraia, L. Cinci, L. Calosi, D. Guasti, L. Pieri, V. Lotti, A. Bonelli, and P. Romagnoli, Forensic Sci Int **244**, 179–185 (2014).
[46] R. Cicchi, S. Sestini, V. De Giorgi, D. Massi, T. Lotti, and F. S. Pavone, Non-linear laser imaging of skin lesions, J. Biophoton. **1**, 62–73 (2008).
[47] A. M. Pena, M. Strupler, T. Boulesteix, and M. C. Schanne-Klein, Opt Express **13**, 6268–6274 (2005).
[48] N. A. Monteiro-Riviere, D. G. Bristol, T. O. Manning, R. A. Rogers, and J. E. Riviere, J. Invest. Dermatol. **95**, 582–586 (1990).